Journal of the Southeastern Association for Research in Astronomy, **7**, 17-22, 2012 December 1

REVERBERATION MAPPING OF AGN DUSTY TORI WITH SPITZER AND IRAC

Kyle F. Twadelle[1,2]
Department of Astronomy, University of Michigan, MI, 48109

Michelle A. Berg[1,2] & Daniel Batcheldor
Department of Physics and Space Sciences, Florida Institute of Technology, FL 32901

ABSTRACT

We report on estimated distances between dusty regions within the tori of three Active Galactic Nuclei (AGN):3C390.3, MRK885, and NGC6418. We present 5 pixel radius aperture photometry of the three AGN, at 3.6 μm and 4.5 μm, using IRAC aboard the Spitzer Space Telescope. 3C390.3 and NGC6418 are found to have sinusoidal trends in their light curves, and time lags between the two wavelengths are used to estimate the distance between these emitting regions of the tori. We also discuss the potential for spacecraft effects of Spitzer that may have created these sinusoidal trends. The time delays between 3.6 μm and 4.5 μ found for 3C390.3 and NGC6418 are 100 $\pm$ 24 days and 8.2 $\pm$ 7.3 days, respectively. Neglecting orientation effects, the corresponding estimated distances between tori regions are 0.084 $\pm$ 0.020 pc and 0.007 $\pm$ 0.006 pc. These estimates are consistent with current constraints on torus size.
Subject headings: galaxies: photometry – galaxies: nuclei – galaxies: Seyfert

1. INTRODUCTION

Active galactic nuclei (AGN) are classified into Type-1 and Type-2, distinguished by the orientation of the AGN to our line-of-sight. The unified model for AGN describes a dusty torus surrounding the central engine, nuclear a broad-line region (BLR) and a more extended narrow-line region (NLR). The BLR consists of gas clouds near the central engine moving at high velocities and emitting broad emission lines. The NLR is located farther away from the central engine and is also made up of gas clouds, but emits narrow emission lines. The central engine of a Type-1 AGN is directly visible due to the orientation of the torus such that it does not obstruct the line-of-sight to the BLR, resulting in visibility of both the BLR and NLR spectra. In contrast, a Type-2 AGN's BLR is obstructed from view by the dusty torus, which is seen edge-on, leaving only the NLR visible and resulting in a lack of broad lines in Type-2 AGN spectra.

The most popular current model is that of a clumpy torus, originally proposed by Elitzur (2006), in which dust is distributed in clumps and possibly surrounded by a smooth, diffuse medium of dust. A model for the torus as homogeneous and smooth was also proposed by Pier & Krolik (1992), but the clumpy model has found success whereas homogeneous models have failed to account for anomalous silicate absorption and emission features (Buchanan et al. 2008). Hydrodynamic models of dusty tori show it to probably be clumpy instead of smooth or continuous, and likely to extend over a few parsecs (Tristram et al. 2007) with a broad distribution of optical depths on the order of $10 \lesssim A_v \lesssim 200$ (Granato et al. 1997).

The accretion disks of Type-1 and Type-2 AGN include UV and optical emissions with these photons being reemitted by the dust of the torus in the infrared (IR) and near-infrared (NIR). Due to the physical distance separating the central engine and the inner radius of the torus, there will be a time delay between the arrivals of the direct accretion disk photons and torus NIR/IR photons. Within the torus, each NIR/IR wavelength emitted corresponds to a distinct dusty region of the torus at a different distance from the accretion disk. The emitting regions of the torus are at varying distances from the central engine, which will result in accretion disk photons taking a different amount of time to reach each region. This creates a time delay between signals received in the NIR/IR wavelengths in which the torus radiates. If signals at different wavelengths match, the time delay will be indicative of the distance light must have traveled from the central engine, before encountering and being re-radiated by the dusty torus. A time delay can also be found between similar signals received from two regions within the torus, indicative of the difference in time it takes for the UV radiation to reach the two regions. Calculations can then place a constraint on the distance between the AGN's central engine and the torus' inner radius, and between two IR-emitting regions within the torus.

The IR emissions from the dusty torus of a sample of 12 AGN were observed by IRAC on the Spitzer Space Telescope once every three days. In this study, IR light curves will be presented for the observed AGN to place constraint on the size of the torus. 3C390.3, NGC6418, and MRK885 will be primary targets in the observations, and data reduction will be performed on the collected images to reveal any variations in the torus emissions. Any such variations found will then be compared to variations found in IR emissions from other regions of the torus and the optical emissions from the AGN central engine (Berg et al., this volume). If there is a correlation found be-

[1] Southeastern Association for Research in Astronomy (SARA) NSF-REU Summer Intern
[2] Visiting observer, SARA Observatory at Kitt Peak, Arizona, which is operated by the Southeastern Association for Research in Astronomy
Electronic address: ktwadell@umich.edu

TABLE 1
Target Information

Target	RA (HMS)	Dec (DMS)	z
MRK885	16:29:48.3	+67:22:42	0.0253
NGC6418	17:38:09.3	+58:42:53	0.0286
3C390.3	18:42:09.0	+79:46:17	0.0561

tween variations in two sets of data, it can be determined whether the IR emissions are lagging other IR emissions or optical emissions. If this is the case, a time "lag" can be found between emissions from two torus regions, or between emissions from the central engine and the corresponding emissions by the torus, resulting from dust re-radiating the light from the central engine. This time "lag" can then be used to place constraints on the distribution of torus material, the distance between the central engine and the inner radius of the torus, and the size of the torus itself.

2. OBSERVATIONS

All observations were performed with the Spitzer Space Telescope's IRAC camera in channels 1 and 2, corresponding to infrared wavelengths of 3.6 μm and 4.5 μm, respectively. An exposure time of 1.2 sec was used in all observations, including those of the comparison star and AGN. Originally the pixel scale was 1.2 arcsec/pixel, but the data was dithered such that the effective pixel scale became 0.6 arcsec/pixel. In total 12 AGN were observed, including 3C390.3, MRK885, and NGC6418 upon which we focuses, and the standard star BD+60 1753. Table 1 lists the coordinates and redshift of the three AGN of interest. Observations were performed over the period 24 April 2011 to 14 June 2012 with a sampling interval of 3 days. No observations of any target were taken with Spitzer during the 30 day period between 3 December 2011 and 2 January 2012 due to continuous observations of NGC2264 that overrode the scheduled time for this project's observations. There is also a gap in observation data of MRK885 from 27 September 2011 to 28 November 2011 as a result of MRK885 being outside of Spitzer's Continuous Viewing Zone.

Problems arose in observations of the guide star BD+60 1753, which showed significant variations in the star's flux density over time, contrary to what should be a relatively constant flux density. The variations were only seen when aperture photometry using a 1.5 pixel radius aperture was used, leading to the conclusion that the variations were a result of an inter-pixel response function (IPRF) due to the small size of the aperture. Therefore, data collected from the 1.5 pixel radius aperture was not used. The variations were not present in photometry performed with a 5 pixel aperture radius, and photometric data collected using this radius is used in this paper.

3. DATA REDUCTION

3.1. *Aperture Photometry*

Once the mosaic images were obtained from observations of the three AGN and guide star BD+60 1753, aperture photometry was performed on both the channel 1 and channel 2 images in IRAF. A point spread function (PSF) was obtained for the images of BD+60

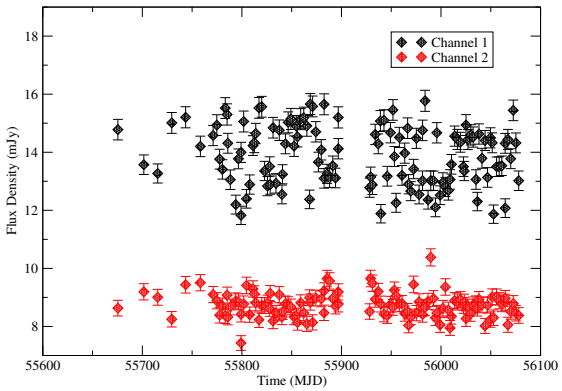

Fig. 1.— Channel 1 (3.6μm) and Channel 2 (4.5μm) light curves for the standard star BD+60 1753, using a photometric aperture radius of 1.5 pixels.

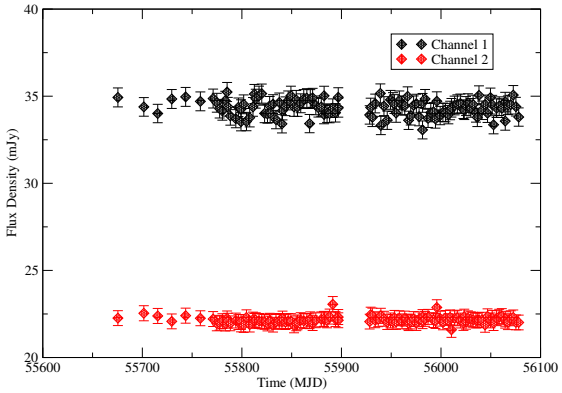

Fig. 2.— As Figure 1 but for an aperture radius of 5 pixels.

1753 and inspected to find its full width at half maximum (FWHM), in order to find an aperture radius that would include the least possible amount of sky, but all of the galaxy. The fitting resulted in an optimal aperture radius of 5 pixels, found by determining where the PSF dropped to the background level. With a 5 pixel radius aperture, any variations observed in the galaxies' flux density profile would be variations in the AGN on top of the galaxy's relatively constant flux. Figures 1 and 2 show the light curve for BD+60 1753, with both channels 1 and 2 for the given aperture radius.

Within IRAF, photometry was performed on the three AGN and BD+60 1753 using the apphot package. The output files created contained photometric information regarding the brightness of the object contained within the aperture. The data included "sum" (total counts including sky in the aperture), "flux" (sky/background-subtracted total counts in the aperture), and "merror" (error in the magnitude in the aperture).

3.2. *Flux Calibration*

After obtaining the image data from aperture photometry the error in counts had to be calculated. Since the error produced by photometry was the error in the magnitude of the aperture, instead of the counts contained within, we recovered the error in counts using

$$\text{error} = \frac{\text{merror} * \text{flux}}{1.0857}. \quad (1)$$

The error was calculated for the "flux" obtained in each time step of observations, measured in Modified Julian

TABLE 2
CALIBRATION DATA

Channel	λ (μm)	K	C ($\frac{MJy/sr}{sec/DN}$)	$FLUXCONV$ ($\frac{MJy/sr}{sec/DN}$)
1	3.6	1.019	0.1088	0.1253
2	4.5	1.001	0.1388	0.1469

Date, and light curves were made for for each target in channels 1 and 2. This data then needed to converted from units of MJy/sr, in which the photometric data was given, to flux density units of mJy. From Reach et al. (2005) on the absolute calibration of IRAC, the conversion (to mJy) is

$$\text{flux} * \text{K} * \text{S} * 10^{-9}(\text{mJy}) \quad (2)$$

$$\text{error} * \text{K} * \text{S} * 10^{-9}(\text{mJy}) \quad (3)$$

where "flux" is the photometric flux output by IRAF in MJy/sr and K is the known dimensionless color correction factor for a channel. Only BD+60 1753 has known K values, so a K value of 1 was assumed for the AGN. In the mosaic images, the area of the square pixels was converted from square arcseconds to steradians following the conversion procedure detailed in the IRAC instrument handbook. The calibrated flux density of BD+60 1753, found using the above conversions, was compared against the star's known flux densities in channels 1 and 2, as recorded in the IRAC instrument handbook. A 10 pixel radius aperture and a 12-20 pixel annulus were used to accurately recover the flux densities in the handbook. Table 2 lists the values of all channel-dependent conversion factors for channels 1 and 2.

4. MODEL FITTING

Once the photometric data for each target was flux calibrated and converted to mJy, flux density was plotted against time for each AGN. In order to highlight variations in the AGN, the difference in flux density between the AGN and BD+60 1753, for each channel, was also plotted. To calculate the difference, an average value for the flux density of BD+60 1753 was found, representing its constant flux density value. The AGN flux density was then subtracted from this value for the corresponding channel, and the absolute magnitude of the difference was used in the resulting plots. To propagate the errors, an average was taken of the guide star error and added to each error in the AGN data. Both channels of each AGN were plotted together in Figures 3-5.

Both 3C390.3 and NGC6418, in channels 1 and 2, showed sinusoidal variations. MRK885 did not appear sinusoidal in either channel. A sinusoidal model was then fitted to individual plots of flux density vs. time for channels 1 and 2 of both AGN, as seen in Figures 3 and 5. A sinusoid-fitting program written in Python was used to make the fits. The sinusoid parameters of amplitude A, period T, and zero crossing point t_0 are listed in Table 3, along with χ^2 values and parameter uncertainties.

5. TIME DELAYS AND CONSTRAINING THE TORUS SIZE

Assuming that the signals received at 3.6 μm and 4.5 μm correspond to two distinct regions of the dusty tori within 3C390.3 and NGC6418, the zero crossing points generated by the sinusoidal fits offer a measurement of

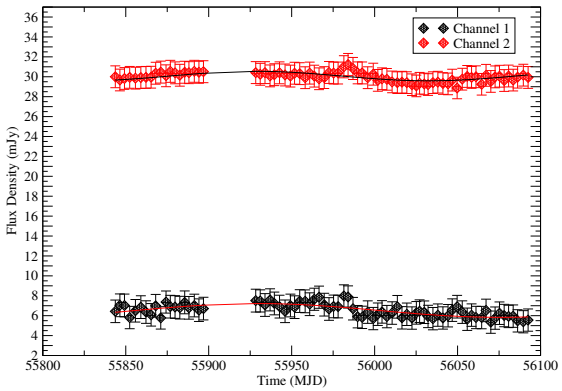

FIG. 3.— Channel 1 (3.6μm) and Channel 2 (4.5μm) light curves for 3C390.3, using a photometric aperture radius of 5 pixels.

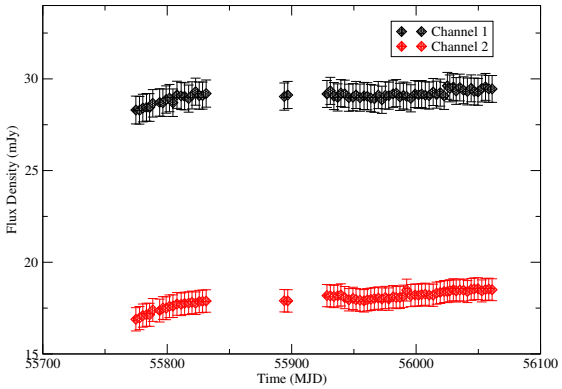

FIG. 4.— Same as Figure 3 but for MRK885.

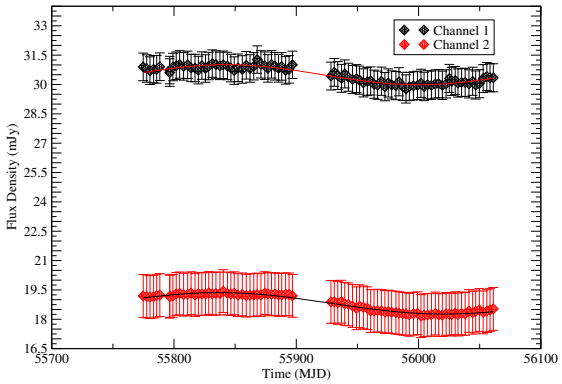

FIG. 5.— Same as Figure 3 but for NGC6418.

the distance between the two emitting regions of the torus. There is a difference in zero crossing points between channels for both AGN, and this is indicative of the relative shift of the sinusoids. This shift is equal to the difference in time needed for the accretion disk radiation to reach the separate regions of the dusty torus that are emitting in the observed wavelengths. Due to light travel times, the distance between the two IR-emitting regions can therefore be calculated as follows:

$$d = c * |t_{0,1} - t_{0,2}| \quad (4)$$

The difference in zero crossing points between channels is the time needed for the central engine's radiation to travel between the two regions of the torus. The calculated time delays, equal to $|t_{0,1} - t_{0,2}|$, were 100 $\pm$ 24

TABLE 3
Sinusoidal Fit Parameters

AGN	Channel	A (mJy)	T (days)	T error (days)	t_0 (days)	t_0 error (days)	χ^2
3C390.3	1	1.335	583	44	55784	18	16.919
3C390.3	2	0.499	235	12	55684	6.0	8.333
NGC6418	1	0.505	324	8.0	55760	4.5	1.323
NGC6418	2	0.552	354	5.6	55751	2.8	0.413

days and 8.2 ± 7.3 days for 3C390.3 and NGC6418, respectively. Errors were derived through propagation of zero crossing point error produced from the sine fit of the data. When these times are inputted into Equation 5, the calculated distance is the physical projected distance between the two emitting regions of the torus. Neglecting inclination effects, the resulting distances between the 3.6 μm and 4.5 μm regions of the tori are 0.084 ± 0.020 pc and 0.007 ± 0.006 pc for 3C390.3 and NGC6418, respectively. The physical radii of tori have been constrained between approximately 1 pc and 6 pc (Alonso-Herrero et al. 2011), and the calculated distances between torus regions are consistent with this constraint. However, the error in calculated distance for NGC6418 is too large for the measurement to support any conclusions drawn on the size of the torus.

6. DISCUSSION AND INTERPRETATIONS

As seen in the above figures, all three AGN clearly vary in flux density in both channels 1 and 2. Some comments on the individual AGN follow.

6.1. *MRK885*

MRK885's flux density levels are consistently greater in channel 1 than in channel 2, and both channels' flux density levels are less than the flux densities of BD+60 1753. MRK885 is also distinguished by a clear increase in signal over roughly 100 days before leveling off and then increasing with a relatively small slope. There is no sign of a sinusoidal trend in either channel.

6.2. *NGC6418*

As with MRK885, NGC6418 flux density values are higher in channel 1 than in channel 2, but are lower than the flux density values of BD+60 1753 for both channels. NGC6418 also shows larger spikes in channel 1 than in channel 2, and a sinusoidal trend is apparent in both channels.

6.3. *3C390.3*

Unlike MRK885 and NGC6418, flux density values are greater in channel 2 than in channel 1 of 3C390.3, and both channels' flux density values are consistently greater than those of BD+60 1753. 3C390.3 also has a redshift of $z = 0.0561$, approximately twice that of MRK885 and NGC6418 despite 3C390.3's higher flux density. This greater distance from Spitzer, combined with larger flux density, is evidence that 3C390.3 is much stronger source of radiation at the 3.6 μm and 4.5 μm wavelengths than MRK885 and NGC6418. In terms of variation, 3C390.3 appears to vary more in channel 1, with relatively larger spikes in signal than in channel 2. Both channels display a peak followed by a dip in signal near the Modified Julian Date of 55975.

6.4. *Sinusoidal Fits*

NGC6418's signal is clearly more sinusoidal than that of 3C390.3, and NGC6418's model has Chi-squared values smaller than those of 3C390.3 by a factor of 10.

There is also support for the possibility that in both channels, 3C390.3 is not actually sinusoidal. This is due not only to poorer model fits than those for NGC6418, but also because of disparity between the channels' periods. Compared to the sinusoidal periods of NGC6418, the periods of 3C390.3 are relatively far apart. Similar periods are expected for the sinusoidal models of channel 1 and 2 signals, because channel 2's sinusoid is a result of a shift in the channel 1 sinusoid.

We discuss three possible explanations for the sinusoidal trend in the AGNs' varying flux density. One is that the data is real, and the sinusoidal variation is a result of the AGN's periodically varying flux density.

6.5. *Spacecraft and Zodiacal Light Effects*

The second possibility is that the data is not real, and the sinusoidal trend observed is due to spacecraft effects of the Spitzer Space Telescope as it moves in its Earth-trailing orbit. A target's signal could periodically increase and decrease depending on how great the target's inclination to the ecliptic is when viewed from Spitzer. If the target is closer to the ecliptic plane, in which Spitzer orbits, the telescope would periodically move towards and away from the target. This could potentially create a false periodicity in the target's signal as Spitzer's changing velocity, if high enough, doppler shifted the spectral lines seen by IRAC in the detected waveband. Depending on the magnitude of the doppler shift, the lines could be shifted outside of the waveband, therefore periodically increasing and decreasing the AGN's signal in the waveband. Also, if the signal's period approached 1 year, the data would be more suspect of being the result of a spacecraft effect, due to Spitzer's 1 year orbital period. If the target is closer to a 90° inclination to the plane of Spitzer's orbit, Spitzer would not be moving towards or away from the target at a velocity large enough to create a significant doppler effect. In this case, at a given time Spitzer would receive approximately the same amount of signal from any position in its orbit, and therefore any periodicity observed in the signal would more likely be a real result of the AGN's varying radiation.

In terms of distance from the ecliptic, NGC6418 is closest with a declination of +58:42:53. NGC6418 also has an approximately year-long period of 354 ± 5.6 days in channel 2, along with a period of 323.9 ± 8.0 days in channel 1. If spacecraft effects of Spitzer's orbit are creating the sinusoidal trends in NGC6418's data, a likely period would be Spitzer's orbital period of 1 year. NGC6418's proximity to the ecliptic, along with periods of roughly 1 year, therefore support the possibility

of spacecraft effects influencing the data. In contrast, if spacecraft effects can be identified by sinusoidal trends with year-long periods, the lack of either of these characteristics in both channels of MRK885 suggests that there may be no significant spacecraft effect in the AGN's data. However, any conclusions on a spacecraft effect should not be made without at least two years worth of data to confirm or deny periodicity.

Spitzer's year-long orbit also results in a third possible explanation for the sinusoidal trends as being caused by the zodiacal light (ZL) observed in the infrared. The ZL is sunlight scattered from dust in the zodiacal cloud, an interplanetary dust cloud in the plane of the solar system. Its location results in the ZL being observed near the ecliptic, and the dust scatters the sunlight in the infrared. The ZL is the largest non-instrumental background source in the infrared.

Measurements of the ZL with IRAC, made by Krick et al. (2012), show the ZL signal to vary sinusoidally with a period of approximately 1 year. As discussed by Krick et al. (2012), the sinusoidal variation is a result of Spitzer's movement in its Earth-trailing orbit. Spitzer spends 6 months below the ecliptic dust plane before moving above the plane for another six months, after which it completes its orbit and moves back below the plane. When Spitzer is below the ecliptic dust plane, a maximum in the ZL signal occurs due to there being a large column density of dust in Spitzer's field of view, scattering more sunlight in the infrared. When Spitzer is traveling above the plane, a smaller column density of dust is viewed and a minimum in the ZL signal occurs. From these maxima and minima in Spitzer's year-long orbit, the sinusoidal ZL signal has a period of 1 year.

When observing in channels 1 and 2 of IRAC, the ZL signal must be taken into account due to its large contribution to non-instrumental sky levels. Krick et al. (2012) find that the ZL makes up approximately 50% and 70% of non-instrumental sky levels in channels 1 and 2, respectively.

It is therefore possible that the sinusoidal ZL signal, composing the majority of non-instrumental sky levels observed by IRAC, could be strong enough in the data to create the sinusoidal trends observed in both channels of 3C390.3 and NGC6418. Paralleling the explanation of the spacecraft effect, a strong ZL effect on NGC6418 is supported by the AGN's approximately year-long sinusoidal periods and proximity to the ecliptic.

More time would have to be given to analyzing the sinusoidal trends in 3C390.3 and NGC6418 to determine whether or not their sinusoids could be caused by the ZL signal. If this is found to be the case, further analysis would involve subtracting the ZL sinusoid from the AGN signals, in order to observe variations in the AGN's brightness that occurred on top of the varying ZL signal.

6.6. *Torus Size*

A caveat of the torus distance measurements is the assumption that the sinusoidal trends in the signals received by Spitzer are real, and not the result of spacecraft effects as discussed above. The validity of these calculations also depend on whether or not the observed signals from 3C390.3 are truly sinusoidal. If the sinusoidal trends observed in 3C390.3 and NGC6418 are not real, then the phase shifts produced by the fit are not products of the varying distributions of dust within the torus.

Although the distances between regions emitting in the IR were calculated with the data collected from Spitzer, distances between the torus and the accretion disk, observed in the visual spectrum by the SARA (Southeastern Association for Research in Astronomy) North Telescope (Berg et al. 2012), could not be calculated. This is due to a lack of overlap between the Spitzer and SARA North data as a result of the telescopes taking observations at different times. There was also no variation found in the Sara North visual data to be compared with or matched to the variation found in the AGN flux density by Spitzer.

7. SUMMARY AND CONCLUSIONS

Using time delay techniques we have estimated the size of a region within the dusty torus of the two AGN 3C390.3 and NGC6418. This was accomplished with observations by the Spitzer Space Telescope's IRAC camera, which observed BD+60 1753, 3C390.3, NGC6418, and MRK885 in channels 1 and 2, corresponding to wavelengths of 3.6 μm and 4.5 μm, respectively.

The data collected showed flux density variations in both channels of the three observed AGN, and the variations in channel 2 were found to lag those in channel 1. The variations observed in 3C390.3 and NGC6418 appeared to have sinusoidal trends. Fitting a sinusoidal model to the light curves produced phase shift values for each sine function, and the difference between the phase shifts of the observed channels corresponded to the light travel time between each IR-emitting region of the torus. Neglecting orientation effects, the two observed regions in the tori of 3C390.3 and NGC6418 were found to be 0.084 ± 0.020 pc and 0.007 ± 0.006 pc apart, respectively. These values are consistent with size constraints on torus radii of approximately 1-6 pc (Alonso-Herrero et al. 2011).

The calculated distances are not conclusive, however, due to multiple caveats involving signal periodicity and torus structure. Spacecraft effects of Spitzer's year-long heliocentric orbit, and/or the sinusoidal ZL signal in the infrared, may have created a false periodicity in the signals of 3C390.3 and NGC6418. 3C390.3's signal may not be not truly sinusoidal, due to a relatively weak sinusoidal fit compared to that of NGC6418. More analysis is required to determine whether the spacecraft or ZL effects occurred. It is also unknown exactly what regions of the torus were observed.

The three observed AGN are part of a larger sample of 12 Type-1 AGN, and observations of the rest of the sample by Spitzer will further constrain the size of dusty tori. More observations in the visual spectrum with ground based telescopes, overlapping the time frame of Spitzer's observations, will also help to constrain torus size, allowing distances to be calculated between central engines and IR-emitting regions. Combining calculations of these"inner" distances with those between regions within the torus, stronger constraints can be placed on the overall shape and size of dusty tori in Type-1 AGN.

This project was funded by the National Science Foundation Research Experiences for Undergraduates (REU)

program through grant NSF AST-1004872.

REFERENCES

Alonso-Herrero, A., Ramos Almeida, C., Mason, R., et al. 2011, ApJ, 736, 82
Berg, M. A., Twadelle, K. F., & Batcheldor, D. 2012, JSARA, 7, 13
Buchanan, C. L., Gallimore, J. F., O'Dea, C. P., Baum, S. A., Axon, D. J., Robinson, A., Noel-Storr, J., Yzaguirre, A., Elitzur, M., Elvis, M., and Tadhunter, C. 2008, Mem. S.A.It., 111, 11
Elitzur, M. 2006, New Astron. Rev., 50, 728
Granato, G. L., Danese, L., & Franceschini, A. 1997, ApJ, 486, 147
Krick, J. E., Glaccum, W. J., Carey, S. J., et al. 2012, ApJ, 754, 53
Krolik, J. H., & Begelman, M. C. 1988, ApJ, 329, 702
Pier, E. A., & Krolik, J. H. 1992, ApJ, 401, 99
Reach, W. T., Megeath, S. T., Cohen, M., et al. 2005, PASP, 117, 978
Tristram, K. R. W., Meisenheimer, K., Jaffe, W., & Cotton, W. D. 2007, IAU Symposium, 238, 93